Building and Environment 47 (2012) 32–39

Contents lists available at ScienceDirect

Building and Environment

journal homepage: www.elsevier.com/locate/buildenv

Particle inhalation and deposition in a human nasal cavity from the external surrounding environment

Xiangdong Li, Kiao Inthavong, Jiyuan Tu*

School of Aerospace, Mechanical and Manufacturing Engineering, RMIT University, PO Box 71, Plenty Road, Bundoora Victoria 3083, Australia

ARTICLE INFO

Article history:
Received 31 January 2011
Received in revised form
21 April 2011
Accepted 23 April 2011

Keywords:
Facial features
Inlet velocity profiles
Particle deposition
Nasal cavity
CFD

ABSTRACT

CFD computations of particle flows in a human nasal cavity were conducted, using two types of inlet velocity profiles at the nostril openings respectively. One type is the widely used uniform inlet velocity profile while the other is a realistic inlet velocity profile extracted from the external environment that is influenced by facial features. The latter type of inlet velocity profiles were obtained through CFD computations of indoor gas-particle flows around a human head geometry containing detailed facial features in an enclosed space. Comparisons were made between the predicted results of airflow field, particle tracks and particle deposition efficiency in the nasal cavity. It was revealed that although the effects of facial features exist only in a small region (10–20 mm) in front of the face, they lead to complicated, and non-uniform velocity profiles at the nostril openings. This discrepancy leads to different predictions of airflow fields and local particle deposition efficiency in the nasal cavity, especially in the anterior regions such as the vestibule and nasal valve. The results may further lead to discrepant health-risk assessments associated with particle inhalation. Therefore, for CFD simulations of particle deposition in the nasal cavity, the inlet velocity profiles induced by facial features are important for more realistic results.

1. Introduction

Airborne contagions such as influenza viruses are easily spread in the public space given the daily occurrence of gatherings in enclosed spaces, e.g. office spaces, lecture theatres, public transport, etc. While it is obvious that manufacturing industries and hospitals are at a higher risk of respiratory health concerns, enclosed environments including transport vehicles are susceptible to the spread of infectious disease outbreaks. For example the recent spate of acute epidemic outbreak of influenza such as the bird flu and SARS, and more specifically the H1N1–swine flu, was assisted by public transportation. During the H1N1 outbreak during March and April of 2009, international air travellers departing from Mexico were unknowingly transporting a novel influenza A (H1N1) virus to cities around the world [1]. Studies of infectious disease transmission in other enclosed environments such as aircraft cabins have shown the influence of moving bodies [2], the surrounding airflow distribution [3], and ventilation systems in a patient ward [4]. Therefore it is evident that characterising the particle transport in hospitals, residential buildings, offices and other public enclosed environments is critically important.

Inhalation of airborne particles leads to the respiratory system being exposed to particle deposition in the fragile regions of the deep lungs where gas exchange takes place. The adverse health responses caused by particle deposition have been widely recognised and been attached a great importance. Since the early 1950s, the particle deposition characteristics and relevant airflow patterns in human nasal cavity have been widely investigated, both experimentally and numerically. Early observations [5] were mainly made in vivo. However, in vivo measurements have many limitations basically due to the complex three-dimensional anatomy and narrowness of nasal passages. To resolve this problem, some in-vitro experimental studies [6,7] were conducted with precise anatomical models of nasal cavities. Since the 1990s, with the development of computed tomography (CT) technology and computational fluid dynamics (CFD), a number of numerical studies [8–13] on gas-particle flows in realistic nasal cavities have been conducted and provided precise data for deeper insight of the nature of nasal airflows. However, most of the investigations have failed in taking into account the external effects outside of the nasal cavity (e.g. the facial features), but only applied simplified and uniform airflow/particle velocity profiles at the inlets (e.g. nostril openings). These simplifications may lead to uncertainty or inaccuracy in translation of the findings back to real life.

* Corresponding author. Tel.: +61 3 9925 6191; fax: +61 3 9925 6108.
E-mail address: jiyuan.tu@rmit.edu.au (J. Tu).

0360-1323/$ – see front matter © 2011 Elsevier Ltd. All rights reserved.
doi:10.1016/j.buildenv.2011.04.032

As pointed out by Doorly et al. [14], the structures outside the nasal cavity have a significant effect on the airflow dynamics within it, especially during inspiration, the shape of the external nose influences flow entering the nostrils. Recently, Anthony et al. [15] investigated the velocity field and particle inhalation associated with two differently shaped adult-sized mannequins using a Laser Doppler anemometry and found that the facial features have an obvious affect on the flow field (up to 20 mm) near the mannequin surface. Also, Heist et al. [16] investigated the airflow around a child-sized mannequin and proved that facial features resulted in a reduction of the horizontal velocity upstream from the nose, although this was limited to 10 mm in front of the nose tip. In order to further study the effects of facial features on the air-particle flow characteristics in the nasal cavity, Croce et al. [8] and Storey-Bishoff et al. [17] adopted in-vitro experimental specimens which encompassed part of the face. More recently, Lee et al. [18] included some of the facial features in their computational model to account for the external surroundings the nostril inlet. Although these investigations did not take into account all of the facial features, they demonstrated that for the purpose of adequate simulation, CFD studies to investigate human aspiration of particles should incorporate the complex features of the human face.

Therefore in this study, the flow field surrounding a human body and the particle inhalation (aspiration efficiency) from nasal inhalation was investigated within an enclosed space, relevant to indoor environments. A full body computational model with a realistic human head geometry containing full facial features was employed. The external flow field and particle tracks, particularly in the near breathing region were first analysed. The resulting velocity profiles of airflow and particle tracks at the nostril openings are presented and then transferred as boundary conditions for a separate human nasal cavity simulation. The predicted results of airflow and particle transport in the nasal cavity obtained from computations using the transferred profiles are compared with those computations using a uniform inlet profile. Predicted deposition sites in the nasal cavity are also presented which can help to quantify the type and level of risk associated with the particle inhalation.

2. Numerical procedures

2.1. Computational models

The computational domain for the external air-particle flow field is shown in Fig. 1, which is representative of an enclosed environment that may be occupied. It has dimensions of 4 m-width × 10 m-depth × 3 m-height and contains a 1.7 m tall human manikin. In order to capture the detailed effects of facial features a realistic human head was generated as an IGES file from FaceGEN Modeller software based on photographic images taken from a male volunteer. The three-dimensional (3D) head contains detailed facial features, such as shaped eyes, nose and mouth. Modifications were made to the computational model where possible, to allow the model dimensions to represent the 50th percentile of a human male, aged between 20 and 65 years old, based on anthropometric data of Tilley [19] (see Table 1). The dimensions of the wind tunnel are created large enough so that the flow field near the humanoid was free from the effects of the no-slip condition of the stationary surrounding walls. Unstructured tetrahedral mesh was adopted with a fine mesh around the mouth, nostril, and other high irregular and complex regions. The mesh-independency was achieved at 1.6 million cells from our previous study [20] which utilized the same geometry model.

The nasal cavity geometry and mesh (Fig. 2) were reconstructed using the commercial grid generator ICEM-CFD (Ansys Inc.) based on CT-scans of a healthy, 25-year old Asian male volunteer, 170 cm height, 75 kg. The computational domain is filled with tetrahedral elements, with fine elements employed in complicated or narrow zones. In addition, a near-wall region consisting of dense prism layer elements was generated in order to capture the near-wall airflow/particle behaviours. An initial model with 260,000 unstructured tetrahedral cells was refined until the skewness of the cells and Y_{plus} value on the walls dropped below 0.8 and 0.78 respectively. The final mesh-independent model consisted of 3.5 million cells. This nasal cavity model is labelled as NC01.

2.2. Fluid flow modelling

For the external airflow simulation, a uniform steady freestream velocity of 0.3 m/s, which is a mean value of airflow speeds in indoor environment according to the comprehensive survey by Baldwin and Maynard [21] was applied at the inlet of the room while a zero-pressure gradient boundary condition was used at the outlet. This lead to the Reynolds number at the room inlet to be $Re_{inlet} = 16433$ and the Re-Normalisation Group (RNG) $k-\epsilon$ model was chosen because of its successful utilization in the simulations of indoor pollutant inhalation [22]. Boundary condition settings at the nostrils have previously been set as a uniform velocity with equal mass flow distribution between the left and right chambers

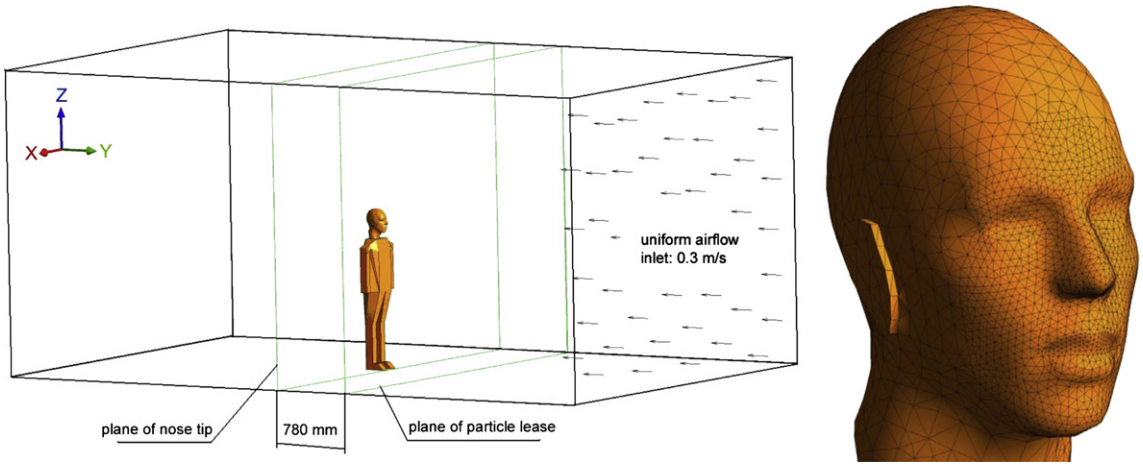

Fig. 1. Computational domain showing a human body in an enclosed environment with a uniform oncoming airflow. An enlarged view of the head shows the computational mesh with refinements in the breathing region of the face.

Table 1
Dimension of the humanoid.

Dimension (cm)	Present study	50 percentile man[a]
Head width	14.0	15.5
Head depth	20.0	19.6
Top of head to chin	23.0	22.1
Location of mouth centre (relative to the top of head)	17.3	18.0

[a] Data taken from Tilley [19].

of the nasal cavity. In contrast, the inhalation process involves a negative pressure build up in the expanding lungs due to the diaphragm muscle contraction pulling downwards. The pressure difference between the atmospheric pressure at the nostrils and the lungs induces inhalation. Furthermore the state of the nasal cavity is dependent on the nasal cycle which is present in more than 80% of normal individuals [23]. This involves the alternating obstruction of one side of the nasal cavity where a physiological congestion of the mucous walls causes enlargement of the mucous, reducing the cross-sectional area and basically creating more resistance in one side of the nasal cavity. Considering that the nasal cavity was reconstructed from CT-scans, the model then represents the state of the nasal cavity at a moment in time, when the scans were taken. Therefore airflow simulations in the nasal cavity were preformed prior to the room simulations to identify the mass flow distribution caused by the differences in the nasal cavity geometry. The nasal cavity was set with a pressure inlet condition at the nostrils ($P_{in} = 0$ Pa) while at the nasopharynx at the outlet of the nasal cavity a pressure outlet condition with a varying negative pressure is used ($P_{out} = \Delta P$ Pa). The resulting mass flow distribution between the left and right chambers of the nasal cavity is shown in Fig. 3. The inhalation rate is set to a steady flow of 15 L per minute (LPM). At this flow rate, the distribution of air through the left and right nostril is 45% and 55% respectively.

The freestream velocity is normal to the face, which is referred to as "facing-the-wind" flow direction. The steady, incompressible Navier–Stokes equations are solved for the airflow. The continuity and momentum equations are given in Eq. (1) and (2) respectively.

$$\nabla\cdot(\rho\vec{U}) = 0 \tag{1}$$

$$\nabla\cdot(\rho\vec{U}\otimes\vec{U}) = \nabla\cdot(\mu+\mu_t)\left(\nabla\vec{U}+(\nabla\vec{U})^T-\frac{2}{3}\delta_{ij}\nabla\cdot\vec{U}\right)-\nabla p \tag{2}$$

where, ρ, $\vec{U}$ and μ are density, velocity and viscosity of the air,

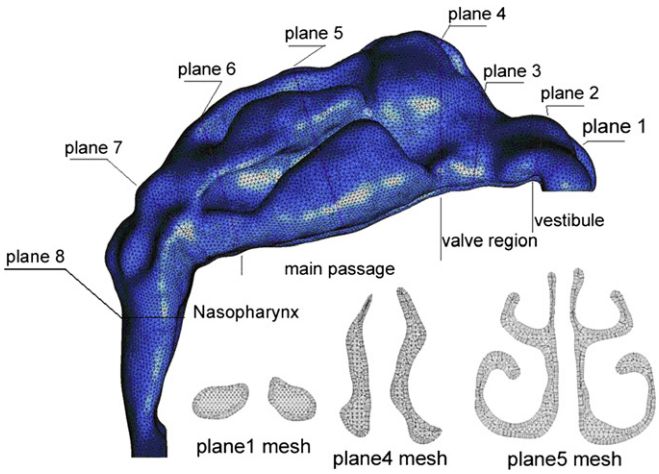

Fig. 2. Geometry and mesh of an internal nasal cavity model labelled as NC01.

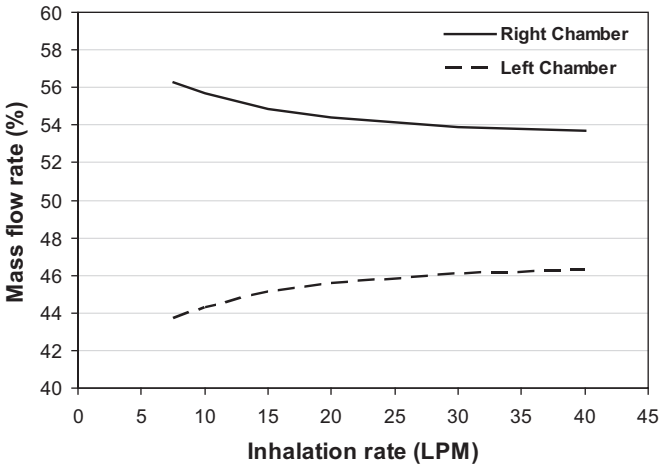

Fig. 3. Mass flow rate distribution between the left and right chambers of the nasal cavity over different steady inhalation rates.

respectively. μ_t is the turbulent viscosity and δ_{ij} is Kronecker delta ($\delta_{ij} = 1$ if $i = j$ and $\delta_{ij} = 0$ if $i \neq j$).

To resolve the boundary layer in the near-wall regions, the Scalable Wall Function [24] was used. The pressure-velocity coupling was resolved using the SIMPLEC algorithm. The convective terms of the transport equations were discretized using second-order-upwind scheme in order to obtain sufficiently accurate solutions. The fluid flow equations were solved in ANSYS CFX 12.1 using a segregated solver with an implicit formulation. The residual values of the transport equations were set to converge at 10^{-5} or below for all simulation cases.

2.3. Particle transport modelling

The particle size in this study was chosen to be in the range of 1–40 μm. In this size range, the gravitational and inertial effect on particle movement are very weak due to the small particle size, and therefore their transport is mostly influenced by the indoor flow field. The particles are tracked through the continuum fluid separately using the Lagrangian approach. For a discrete particle, the forces acting on it that affect the particle acceleration may include the drag force $\vec{F}_D$, buoyancy force $\vec{F}_B$, virtual mass force $\vec{F}_{VM}$, and pressure gradient force $\vec{F}_P$, etc. However, for micron sized particles with high density, the terms that depend on the density ratio are negligibly small. As a result, only the drag force $\vec{F}_D$ and the buoyancy force $\vec{F}_B$ are considered in this study and the equation of particle motion is given by

$$m_p\frac{d\vec{U}_p}{dt} = \vec{F}_D + \vec{F}_B \tag{3}$$

The drag force and buoyancy force are defined by

$$\vec{F}_D = \frac{1}{2}C_D\rho A_p|\vec{U}-\vec{U}_p|(\vec{U}-\vec{U}_p) \tag{4}$$

$$\vec{F}_B = (m_p - m)\vec{g} = \frac{\pi}{6}d_p^3\left(\rho_p-\rho\right)\vec{g} \tag{5}$$

where, m_p, $\vec{U}_p$, and d_p are the particle mass, velocity and diameter, respectively, A_p is the projected area in the flow direction. The drag coefficientC_D is modelled using the Schiller–Naumann correlation [25]. Additional details of the Lagrangian particle modelling have been highlighted in our previous study [20] and will not be repeated here.

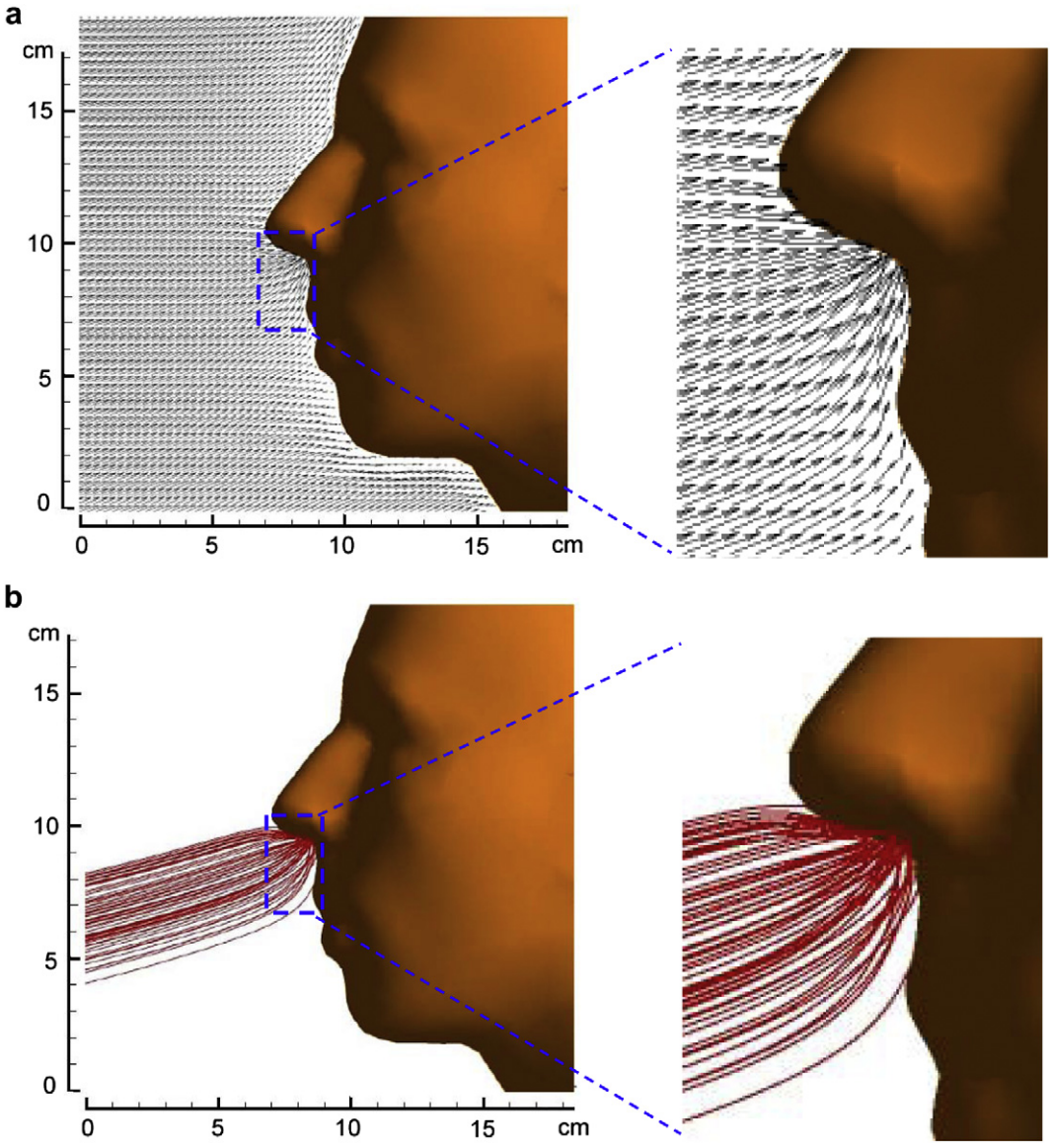

Fig. 4. Airflow vectors and particle tracks in the breathing zone (a) Airflow velocity vectors (b) particle tracks.

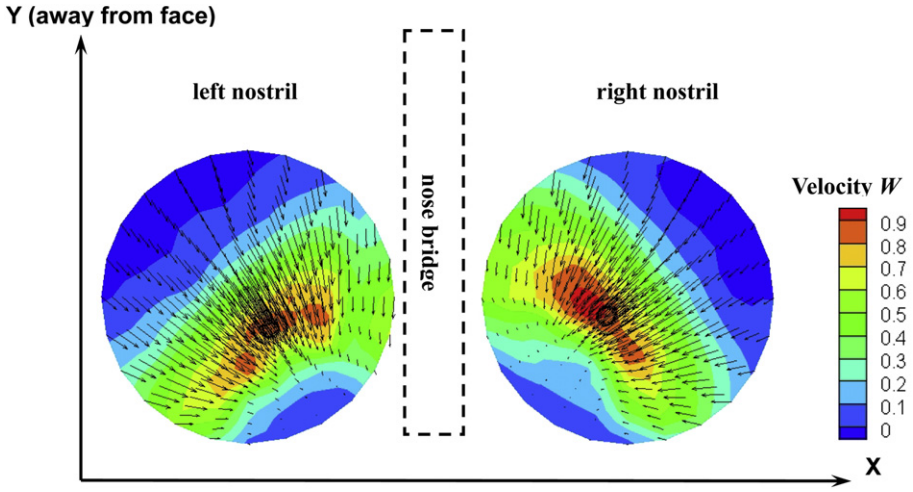

Fig. 5. *W*-velocity contour profiles overlayed with cross-flow vectors of *U*–*V* velocity. View perspective is in the negative *Z*-direction which is from above (superior to) the head looking down through the nostril openings (see Fig. 1 for coordinate system).

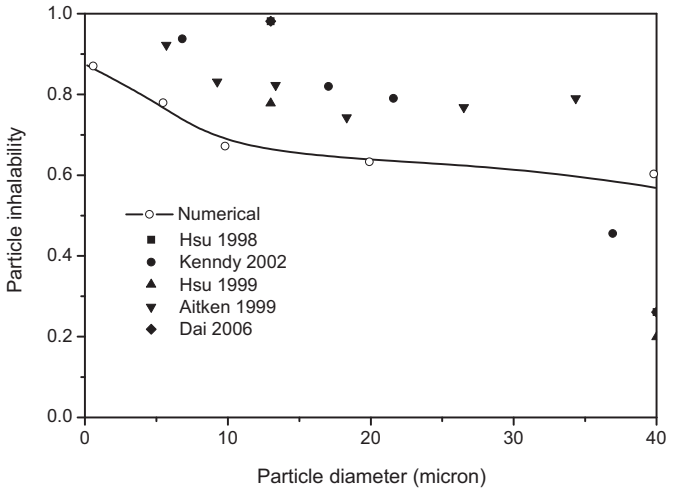

Fig. 6. Particle inhalability by nasal inhalation at 15 LPM.

Particles with the density of 1000 kg/m^3 are released in a plane 780 mm in front of the nose tip. To achieve a uniform particle concentration assumption and to satisfy the "negligible bluff-off effects" criteria proposed by Chung et al. [26], the particles were released at the same velocity as that of the freestream (0.3 m/s). The number of particles tracked was checked for statistical independence and this was determined by repeated simulations where the number of particles was increased until the inhalation efficiency became independent of the number of particles. Independence was achieved for 30,000 particles since an increase to 50,000 particles yielded a difference less than 0.1% in the inhalation efficiency.

3. Results and discussion

3.1. Airflow in the breathing zone and particle inhalation

The flow field computation has been conducted for mouth inhalation previously by the authors in [20] which showed good comparisons against the Laser Doppler Anemometry experimental data of Anthony et al. [15]. For brevity the results are not reprinted here. It is noted that both the previous and present studies utilized the same geometry model, boundary conditions and numerical procedures, therefore despite no direct experimental evidence available to validate the flow field in the present study, it is still reasonable to believe that the flow field prediction in the present study is accurate. The airflow velocity vectors around the human head for nasal inhalation are shown in Fig. 4(a), which illustrates that due to presence of the human head, the airflow changes its direction around 1–2 cm in front of the face outline. The airflow under the nose accelerates, converging into the nostril openings. Immediately before entering the nostrils, the inhaled airflows through a small region bounded by the nostril openings and the philtrum, in which it acutely changes its direction to fit the nostril geometries. Similarly, particle tracks in this region also have large flow curvatures before the particles enter the nostrils (Fig. 4b). As a result of this, both the airflow and particle tracks have complicated velocity profiles at the nostril openings, that are not uniform and perpendicular to the nostril openings. Fig. 5 illustrates the airflow velocity profiles at the both nostril openings, where the coordinate X points from the left-hand-side to the right-hand-side, the coordinate Y points away from the face, and the coordinate Z is positive into the nasal cavity. It was found that in the major area of the both nostril openings, the cross-flow component of the airflow velocity (U–V velocity $= \sqrt{U^2+V^2}$) points towards the corner of nose bridge and philtrum. However, in the area where the nostrils attach to the upper lip and philtrum, the axial velocity and cross-flow velocity components are low. In addition, the vertical component of airflow velocity (W) also has a complicated distribution, where the maximum value is not located at the centre, but slightly skewed towards the nose bridge corner. Similarly, the particle tracks have an analogous distribution at the nostril openings. As a result, it can be safely concluded that both the airflow and particle tracks have complicated velocity profiles, and are not equally distributed at the nostril openings.

The particle inhalability η or aspiration efficiency is the ratio of the inhaled particle concentration to the ambient freestream particle concentration using a so-called "critical area" [27] defined by:

$$\eta = \frac{A_C V_C}{A_n V_n} \tag{6}$$

where, A_C and V_C are the critical area and the airflow velocity in the critical area, A_n and V_n are the inhalation area and the average inhalation velocity, respectively.

Comparison of the predicted particle inhalability against the experimental data available in the literature is shown in Fig. 6. The numerical results generally agree with the experimental data but are slightly lower when the particle diameter is small ($\leq$30 μm) while larger than the experimental data when the particle diameter is larger than 30 μm. This is perhaps due to the transition in particle transport mechanisms with increasing particle size. Zhu et al. [28] and Dai et al. [29] found out that the gravitational or inertial effects on particles of diameter of 30 μm or less are negligible due to their

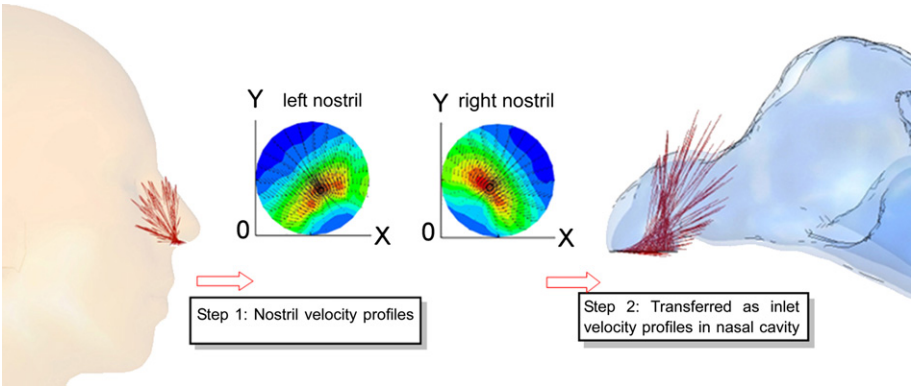

Fig. 7. Transfer of velocity components u, v, w taken from the nostril outlet in the room simulation to the nostril inlets in the internal nasal cavity simulation.

Table 2
Air velocity components at the nostril openings.

	Left nostril			Right nostril		
	U	*V*	*W*	*U*	*V*	*W*
a	8.2423e2	3.4353e1	−4.1179e1	5.0449e1	3.7888e1	−3.1948e1
b	3.2013e1	−7.2404e1	1.1768e2	−3.6865e1	−1.6757e2	2.6415e2
c	−1.6052e1	−1.3226e2	3.3323e2	−2.6632e2	−1.9754e0	3.4864e2
d	−2.3896e4	3.3222e2	−4.8379e3	−2.8867e4	2.2502e4	−4.5843e4
e	−2.1169e4	−1.0160e3	−6.8721e4	4.2215e4	−4.3915e4	−5.4659e4
f	2.3012e6	7.8828e5	−4.6681e5	3.0455e6	−6.1538e5	1.6079e6
g	2.6323e6	1.2957e6	3.5616e6	−1.4191e6	4.5819e6	1.6082e6

small size, and therefore their transport is mostly influenced by the indoor flow field. For particles over 30 μm, the inertial effect gradually comes to play. Despite this, the numerical computations of particle inhalability presents more realistic boundary conditions and leads to a more accurate prediction of the particle deposition in the nasal cavity, which will be discussed in the following sections.

3.2. Airflow and particle deposition in the nasal cavity

The velocity profiles at the nostrils obtained from the room simulation are extracted and a polynomial surface fit is applied each of the velocity components using Matlab. The 2D *X*–*Y* coordinate system is reset where the minimum *X* and *Y* values are set to zero for easy transfer from the room model to the internal nasal cavity model (Fig. 7). Then equations for each velocity components are fitted with the following generic formula:

$$u_i = a + bx + cy + dx^2 + ey^2 + fx^3 + gy^3 \quad (7)$$

where u_i represent *U*, *V* and *W*, respectively. *x* and *y* are local *X* and *Y* coordinates for each nostril opening, respectively. Values of the coefficients *a*, *b*, *c*, *d*, *e*, *f* and *g* are listed in Table 2. The resultant velocity components' profiles at the nostril inlets are shown in Fig. 8. By separating the individual velocity components, the airflow pattern at the inlets becomes more descriptive.

In order to study the effects of inlet boundary conditions caused by the facial features, computations with the same flow rate and particle numbers but uniform inlet velocity boundary conditions are also conducted for the purpose of comparison. In the following sections, the "realistic boundary conditions" and the "uniform boundary conditions" are referred as "Realistic" and "Uniform", respectively. Differences in the inlet velocity profiles will lead to variations in the predicted results of airflow velocity and particle deposition patterns in the nasal cavity. To make a thorough analysis of the effects of inlet boundary conditions, the airflow velocity profiles in plane 1, 2, 3, and 4 are illustrated in Fig. 9. It can be seen that in the anterior parts of the nasal cavity, obvious difference exists between the airflow velocity fields from the two inlet boundary conditions. For example in Plane 1 (in the middle of the vestibule), the Realistic condition yielded vortices in both the vestibule chambers and a higher cross-flow velocity gradient in the right vestibule, while the Uniform condition did not yield any visible vortices and brought up an evenly distributed cross-flow velocity. In Plane 2 which is located near the nasal valve region, the Realistic condition yielded vortices in both chambers while the Uniform condition yielded weak cross-flows. However, in Plane 3 and Plane 4 the difference between the airflow velocity profiles begin to weaken. It is found that in Plane 3 only a small difference exists in the velocity profiles in the left chamber, while no obvious difference can be detected in the right one. In Plane 4 (in front of the main passage) and further downstream posterior planes (not shown in Fig. 8), both types of boundary conditions yield almost the same airflow velocity profiles. This suggests that the influence of the inlet profile is limited to the anterior third of the nasal cavity while downstream it recovers from any inlet variations and is only affected by the nasal cavity geometry thereafter.

Fig. 10 shows the comparison of particle tracks (particle diameter 1, 25 and 40 μ) yielded from the two inlet boundary conditions. It can be seen that the Realistic conditions yield a more dispersed

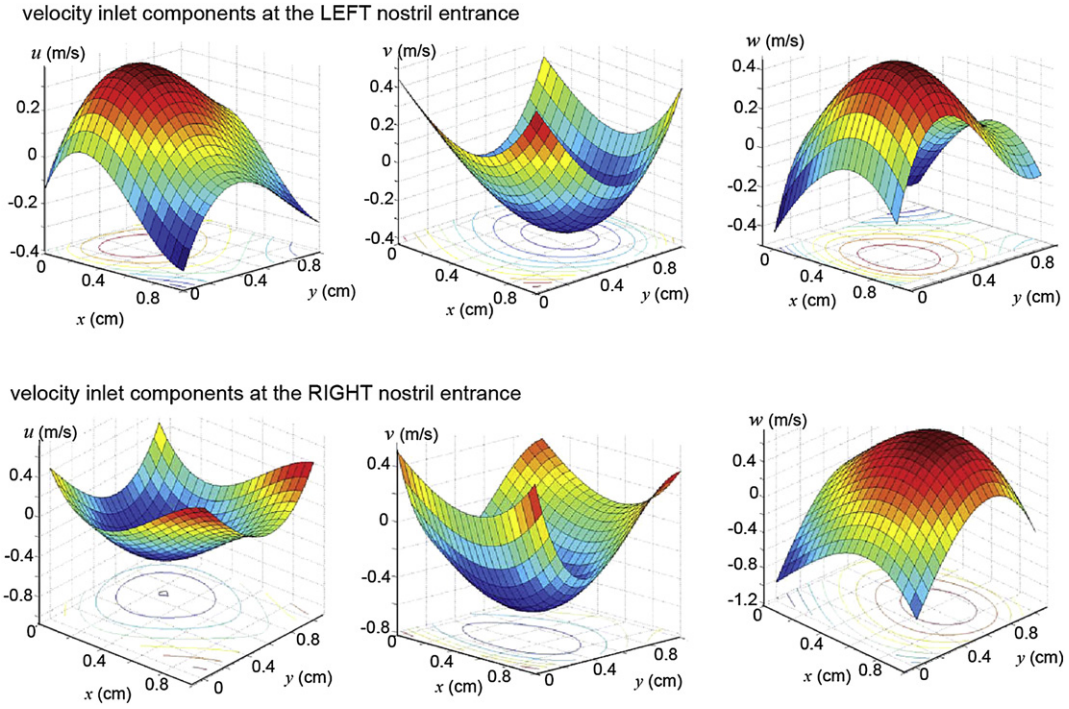

Fig. 8. Individual velocity components' (*u*, *v*, *w*) profiles showing the non-uniform behaviour during inhalation.

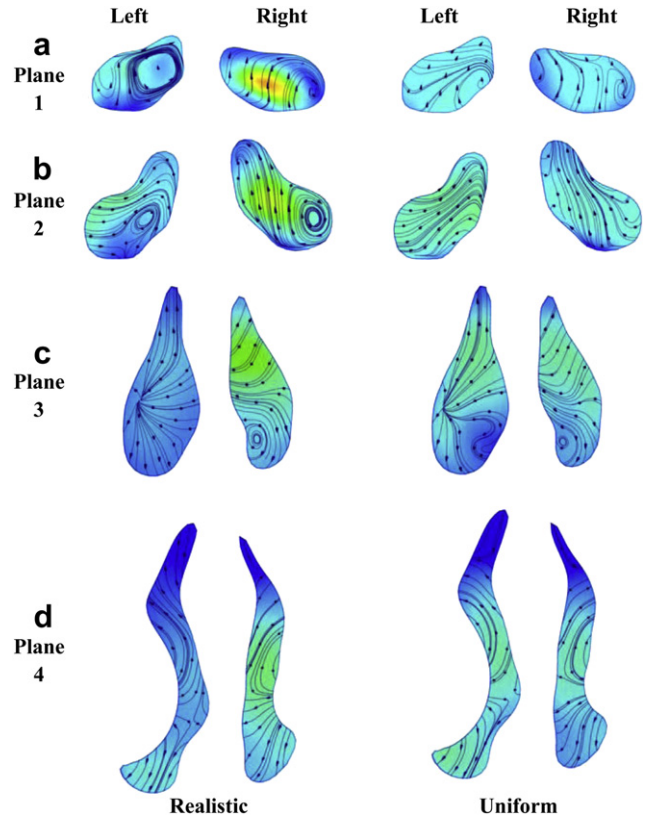

Fig. 9. Comparison of airflow velocity contour and cross-flow streamlines in the anterior parts of the nasal cavity.

particle track profile throughout the nasal cavity, despite the particle size. This is because when a Realistic condition is employed, the airflow velocity contains more dispersed velocity components at the inlet, which directly influences the particle movement and

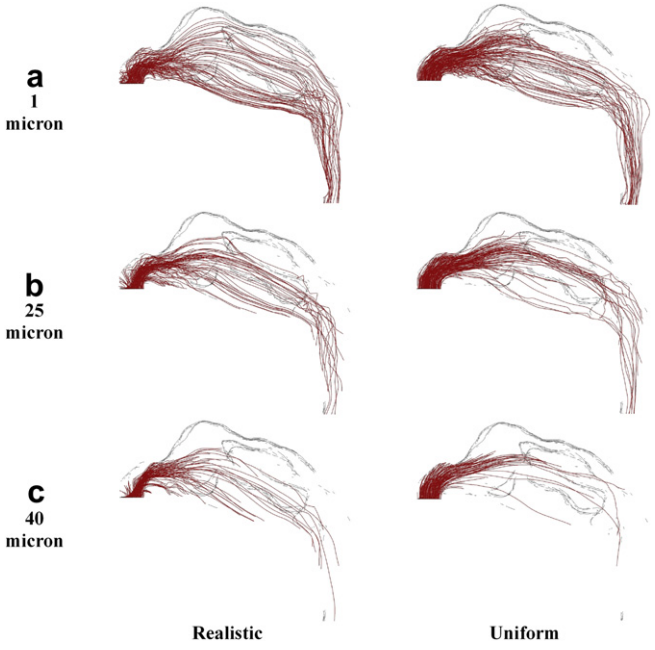

Fig. 10. Comparison of particle trajectory for 1, 25, and 40 μ sized particles in the nasal cavity.

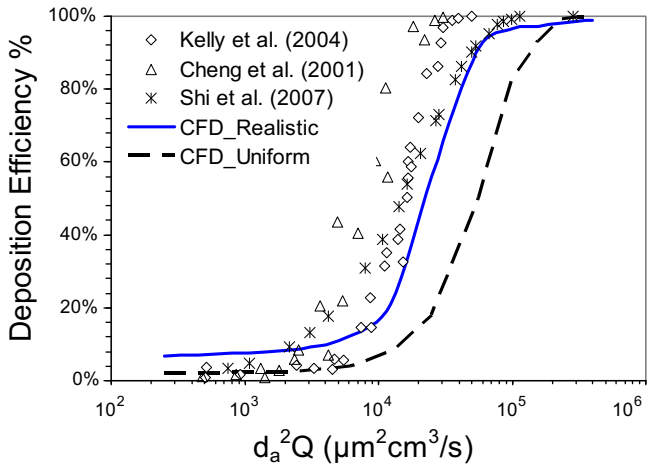

Fig. 11. Deposition efficiencies for particles between 1 and 40 μm and a constant inspiratory flow rate of 15 LPM as a function of the impaction parameter, d_a^2Q.

transport. While similar airflow fields are found in the middle and posterior region of the nasal cavity, different predictions of particle movement and locations in the anterior part will inevitably lead to different particle trajectory and final deposition in the middle and posterior parts. Furthermore, it is also noticed that the Realistic condition leads to higher total particle deposition efficiency in the whole particle size range of 1–40 μ. Fig. 11 illustrates the overall particle deposition efficiency vs. the Inertial Parameter by IP = d_a^2Q, where d_a^2 is the aerodynamic particle diameter in microns and Q is the airflow rate in cm^3/s. The numerical results are also compared with the experimental data from Kelly et al. [30], Cheng et al. [31] and Shi et al. [11]. Fig. 11 shows that the particle deposition efficiency curve shifts to the left when using the Realistic condition in comparison with the Uniform boundary condition. The difference in particle deposition efficiency predictions caused by the inlet boundary conditions will unavoidably lead to different risk assessment relevant to particle inhalation and deposition. Therefore, it is important to take into account the velocity profiles at the nostril openings caused by facial features when numerically simulating gas-particle flows in the nasal cavity.

4. Conclusions

Particle inhalation by human nasal inspiration in indoor environment was numerically simulated by employing a realistic human head geometry. Importance was attached to the effects of facial features on the airflow velocity profile and particle tracks near the nostril openings. Then, numerical results of both the airflow velocity and particle track profiles at the nostril openings were transferred as the inlet velocity boundary conditions to the simulations of particle deposition in the nasal cavity. For the purpose of comparison, the uniform velocity boundary conditions which have been widely used in the simulations of gas-particles flows in human nasal cavity were also adopted in the computations. Comparison between the numerical results revealed that although the facial features have only a small affecting region near the breathing zone, they lead to complicated airflow and particle track velocity profiles at the nostril openings.

Compared with the uniform airflow and particle injection into the nostril openings, the realistic boundary conditions caused by facial features leads to stronger vortex flow in the anterior region of nasal cavity, especially in the vestibule and nose valve regions. Although the realistic and uniform boundary conditions yield

similar airflow profiles in the middle and posterior parts of the nasal cavity, there are significant differences in particle deposition patterns and particle deposition efficiencies. This will inevitably lead to different assessment results relevant to particle inhalation and deposition.

Conflict of interest statement

The authors all declare that there is no potential conflict of interest including any financial, personal or other relationships with other people or organizations within that could inappropriately influence (bias) this work.

Acknowledgements

The financial support provided by the Australian Research Council (project ID LP0989452 and LP110100140) and by RMIT University through an Emerging Researcher Grant are gratefully acknowledged.

References

[1] Khan K, Arino J, Hu W, Raposo P, Sears J, Calderon F, et al. Spread of a novel influenza A (H1N1) virus via Global Airline Transportation. New England Journal of Medicine 2009;361:212–4.
[2] Poussou S, Mazumdar S, Plesniak MW, Sojka P, Chen Q. Flow and contaminant transport in an airliner cabin induced by a moving body: scale model experiments and CFD predictions. Atmospheric Environment 2010;44:2830–9.
[3] Zhang Z, Chen X, Mazumdar S, Zhang T, Chen Q. Experimental and numerical investigation of airflow and contaminant transport in an airliner cabin mockup. Building and Environment 2009;44:85–94.
[4] Yin Y, Xu W, Gupta JK, Guity A, Marmion P, Manning A, et al. Experimental study on displacement and mixing ventilation systems for a patient ward. HVAC&R Research 2009;15:1175–91.
[5] Proetz AW. Air currents in the upper respiratory tract and their clinical importance. The Annals of Otology, Rhinology & Laryngology 1951;60:439–67.
[6] Chung SK, Kim SK. Digital particle image velocimetry studies of nasal airflow. Respiratory Physiology & Neurobiology 2008;163:111–20.
[7] Hahn I, Scherer PW, Mozell MM. Velocity profiles measured for airflow through a large-scale model of the human nasal cavity. Journal of Applied Physiology 1993;75:2273–87.
[8] Croce C, Fodil R, Durand M, Sbirlea-Apiou G, Caillibotte G, Papon JF, et al. In vitro experiments and numerical simulations of airflow in realistic nasal airway geometry. Annals of Biomedical Engineering 2006;34:997–1007.
[9] Inthavong K, Wen J, Tian ZF, Tu JY. Numerical study of fibre deposition in a human nasal cavity. Journal of Aerosol Science 2008;39:253–65.
[10] Liu Y, Matida EA, Johnson MR. Experimental measurements and computational modeling of aerosol deposition in the Carleton-Civic standardized human nasal cavity. Journal of Aerosol Science 2010;41:569–86.
[11] Shi HW, Kleinstreuer C, Zhang Z. Modeling of inertial particle transport and deposition in human nasal cavities with wall roughness. Journal of Aerosol Science 2007;38:398–419.
[12] Wang SM, Inthavong K, Wen J, Tu JY, Xue CL. Comparison of micron- and nanoparticle deposition patterns in a realistic human nasal cavity. Respiratory Physiology & Neurobiology 2009;166:142–51.
[13] Wen J, Inthavong K, Tu JY, Wang S. Numerical simulations for detailed airflow dynamics in a human nasal cavity. Respiratory Physiology & Neurobiology 2008;161:125–35.
[14] Doorly DJ, Taylor DJ, Schroter RC. Mechanics of airflow in the human nasal airways. Respiratory Physiology & Neurobiology 2008;163:100–10.
[15] Anthony TR, Flynn MR, Eisner A. Evaluation of facial features on particle inhalation. Annals of Occupational Hygiene 2005;49:179–93.
[16] Heist DK, Eisner AD, Mitchell W, Wiener R. Airflow around a child-size Manikin in a low-speed wind environment. Aerosol Science and Technology 2003;37:303–14.
[17] Storey-Bishoff J, Noga M, Finlay WH. Deposition of micrometer-sized aerosol particles in infant nasal airway replicas. Journal of Aerosol Science 2008;39:1055–65.
[18] Lee J-H, Na Y, Kim S-K, Chung S-K. Unsteady flow characteristics through a human nasal airway. Respiratory Physiology & Neurobiology 2010;172:136–46.
[19] Garcia GJM, Tewksbury EW, Wong BA, Kimbell JS. Interindividual variability in nasal filtration as a function of nasal cavity geometry. Journal of Aerosol Medicine and Pulmonary Drug Delivery 2009;22:139.
[20] King Se CM, Inthavong K, Tu J. Inhalability of micron particles through the nose and mouth. Inhalation Toxicology 2010;22:287–300.
[21] Baldwin PEJ, Maynard AD. A survey of wind speeds in indoor workplaces. The Annals of Occupational Hygiene 1998;42:303–13.
[22] Birda AJ. Use of numerical calculations to simulate the sampling efficiency performance of a personal aerosol sampler. Aerosol Science and Technology 2005;39:15.
[23] Keay D, Smith I, White A, Hardcastle PF. The nasal cycle and clinical examination of the nose. Clinical Otolaryngology & Allied Sciences 1987;12:345–8.
[24] Mühlfeld C, Gehr P, Rothen-Rutishauser B. Translocation and cellular entering mechanisms of nanoparticles entering mechanisms of nanoparticles. Swiss Medical Weekly; 2008:138.
[25] Schiller L, Naumann Z. A drag coefficient correlation. Zeitschrift Des Vereines Deutscher Ingenieure; 1935:77.
[26] Chung IP, Trinh T, Dunn-Rankin D. Experimental investigation of a two-dimensional cylindrical sampler. Journal of Aerosol Science 1994;25:935–55.
[27] Anthony TR, Flynn MR. Computational fluid dynamics investigation of particle inhalability. Journal of Aerosol Science 2006;37:750–65.
[28] Zhu S, Kato S, Yang J-H. Study on transport characteristics of saliva droplets produced by coughing in a calm indoor environment. Building and Environment 2006;41:1691–702.
[29] Dai YT, Juang YJ, Wu YY, Breysse PN, Hsu DJ. In vivo measurements of inhalability of ultralarge aerosol particles in calm air by humans. Journal of Aerosol Science 2006;37:967–73.
[30] Kelly JT, Asgharian B, Kimbell JS, Wong BA. Particle deposition in human nasal airway replicas manufactured by different methods. Part 1: inertial regime particles. Aerosol Science Technology 2004;38:1063–71.
[31] Cheng YS, Holmes TD, Gao J, Guilmette RA, Li S, Surakitbanharn Y, et al. Characterization of nasal spray pumps and deposition pattern in a replica of the human nasal airway. Journal of Aerosol Medicine 2001;14:267–80.